



Universiteit  
Leiden  
The Netherlands

## **Transient obscuration event captured in NGC 3227. II. Warm absorbers and obscuration events in archival XMM-Newton and NuSTAR observations**

Wang, Y.; Kaastra, J.; Mehdipour, M.; Mao, J.; Costantini, E.; Kriss, G.A.; ... ; He, Z.

### **Citation**

Wang, Y., Kaastra, J., Mehdipour, M., Mao, J., Costantini, E., Kriss, G. A., ... He, Z. (2022). Transient obscuration event captured in NGC 3227. II.: Warm absorbers and obscuration events in archival XMM-Newton and NuSTAR observations. *Astronomy & Astrophysics*, 657. doi:10.1051/0004-6361/202141599

Version: Publisher's Version


License: [Creative Commons CC BY 4.0 license](https://creativecommons.org/licenses/by/4.0/)

Downloaded from: <https://hdl.handle.net/1887/3515576>

**Note:** To cite this publication please use the final published version (if applicable).

# Transient obscuration event captured in NGC 3227

## II. Warm absorbers and obscuration events in archival *XMM-Newton* and *NuSTAR* observations

Yijun Wang (王倚君)<sup>1,2,3,4,5,6</sup> , Jelle Kaastra<sup>2,1</sup>, Missagh Mehdipour<sup>10,2</sup>, Junjie Mao (毛俊捷)<sup>7,8,2</sup>, Elisa Costantini<sup>2,9</sup>, Gerard A. Kriss<sup>10</sup>, Ciro Pinto<sup>11</sup>, Gabriele Ponti<sup>12,13</sup>, Ehud Behar<sup>14</sup>, Stefano Bianchi<sup>15</sup>, Graziella Branduardi-Raymont<sup>16</sup>, Barbara De Marco<sup>17</sup>, Sam Grafton-Waters<sup>16</sup>, Pierre-Olivier Petrucci<sup>18</sup>, Jacobo Ebrero<sup>19</sup>, Dominic James Walton<sup>20</sup>, Shai Kaspi<sup>21</sup>, Yongquan Xue (薛永泉)<sup>3,4</sup>, Stéphane Paltani<sup>22</sup>, Laura di Gesu<sup>23</sup>, and Zhicheng He (何志成)<sup>3,4</sup>

(Affiliations can be found after the references)

Received 20 June 2021 / Accepted 7 October 2021

### ABSTRACT

The relationship between warm absorber (WA) outflows of active galactic nuclei and nuclear obscuration activities caused by optically thick clouds (obscurers) crossing the line of sight is still unclear. NGC 3227 is a suitable target for studying the properties of both WAs and obscurers because it matches the following selection criteria: WAs in both ultraviolet (UV) and X-rays, suitably variable, bright in UV and X-rays, and adequate archival spectra for making comparisons with the obscured spectra. In the aim of investigating WAs and obscurers of NGC 3227 in detail, we used a broadband spectral-energy-distribution model that is built in findings of the first paper in our series together with the photoionization code of SPEX software to fit the archival observational data taken by *XMM-Newton* and *NuSTAR* in 2006 and 2016. Using unobscured observations, we find four WA components with different ionization states ( $\log \xi$  [erg cm s<sup>-1</sup>]  $\sim -1.0, 2.0, 2.5, 3.0$ ). The highest-ionization WA component has a much higher hydrogen column density ( $\sim 10^{22}$  cm<sup>-2</sup>) than the other three components ( $\sim 10^{21}$  cm<sup>-2</sup>). The outflow velocities of these WAs range from 100 to 1300 km s<sup>-1</sup>, and show a positive correlation with the ionization parameter. These WA components are estimated to be distributed from the outer region of the broad line region (BLR) to the narrow line region. It is worth noting that we find an X-ray obscuration event in the beginning of the 2006 observation, which was missed by previous studies. We find that it can be explained by a single obscurer component. We also study the previously published obscuration event captured in one observation in 2016, which needs two obscurer components to fit the spectrum. A high-ionization obscurer component ( $\log \xi \sim 2.80$ ; covering factor  $C_f \sim 30\%$ ) only appears in the 2016 observation, which has a high column density ( $\sim 10^{23}$  cm<sup>-2</sup>). A low-ionization obscurer component ( $\log \xi \sim 1.0-1.9$ ;  $C_f \sim 20\%-50\%$ ) exists in both 2006 and 2016 observations, which has a lower column density ( $\sim 10^{22}$  cm<sup>-2</sup>). These obscurer components are estimated to reside within the BLR by their crossing time of transverse motions. The obscurers of NGC 3227 are closer to the center and have larger number densities than the WAs, which indicate that the WAs and obscurers might have different origins.

**Key words.** X-rays: galaxies – galaxies: active – galaxies: Seyfert – galaxies: individual: NGC 3227 – techniques: spectroscopic

### 1. Introduction

Active galactic nuclei (AGN) accrete matter onto a central supermassive black hole (SMBH) to produce intense broadband radiation, which can ionize and drive away the surrounding matter in form of outflows. Many observational proofs have implied that outflows might play an important role in affecting the star formation and evolution of their host galaxies (see the review of King & Pounds 2015). Ionized outflows can be detected via absorption features along the line of sight in the ultraviolet (UV) and X-rays, which usually have different types (Laha et al. 2021, and references therein) such as broad absorption lines (BALs; Weymann et al. 1981), warm absorbers (WAs; Halpern 1984; Crenshaw et al. 2003), and ultrafast outflows (UFOs; Tombesi et al. 2010). Such UFOs might have an origin close to the central engine ( $\sim 0.0003-0.03$  pc; Tombesi et al. 2012), with very high velocities ( $\sim 0.03-0.3c$ ; Tombesi et al. 2010, 2012). The BALs usually reside outside the broad line region (BLR) with high outflow velocities reaching  $\sim 30\,000$  km s<sup>-1</sup> (Trump et al. 2006; Gibson et al. 2009). Compared with UFOs and BALs, WAs have lower outflow velocities from about one hundred to

several thousand km s<sup>-1</sup> (Kaastra et al. 2000; Ebrero et al. 2013) and they might originate in the accretion disk (e.g., Elvis 2000; Krongold et al. 2007), BLR (Reynolds & Fabian 1995), or dusty torus (e.g., Krolik & Kriss 2001; Blustin et al. 2005). Although different types of outflows have overlaps in their distance scales and outflow parameters, the direct connection between these outflows still remains unclear. In this work, we mainly focus on the properties of the WA outflows.

According to Tarter et al. (1969), the ionization parameter can be defined by

$$\xi = \frac{L_{\text{ion}}}{n_{\text{H}} r^2}, \quad (1)$$

where  $L_{\text{ion}}$  is the ionizing luminosity over 1–1000 Ryd,  $n_{\text{H}}$  is the hydrogen number density of the absorbing gas, and  $r$  is the radial distance of the absorbing gas to the central engine. The WAs might be driven by radiation pressure (e.g., Proga & Kallman 2004), magnetic forces (e.g., Blandford & Payne 1982; Konigl & Kartje 1994; Fukumura et al. 2010), or thermal pressure (e.g., Begelman et al. 1983; Krolik & Kriss 1995;

Mizumoto et al. 2019), and show a wide range of ionization parameter ( $10^{-1} \leq \xi \leq 10^3 \text{ erg cm s}^{-1}$ ) and hydrogen column density ( $10^{20} \leq N_{\text{H}} \leq 10^{23} \text{ cm}^{-2}$ ) (Laha et al. 2014). Investigating properties of WAs can help us to understand the formation of AGN outflows and their feedback efficiency to the host galaxy. These WAs have been found in about 50% of nearby AGN (e.g., Reynolds 1997; Kaastra et al. 2000; Porquet et al. 2004; Tombesi et al. 2013; Laha et al. 2014), and the properties of WAs show differences among different AGN, such as the different ionization states, column densities, and outflow velocities (Tombesi et al. 2013; Laha et al. 2014).

Moreover, the X-ray spectra of some AGN present dramatic hardening accompanied by flux-drops on short timescales, which might be due to the X-ray transient obscuration events (Markowitz et al. 2014). Transient obscuration events can also cause absorption features in the soft X-ray and UV bands, which usually appear and disappear on shorter timescales, as compared with outflows. These obscuration events might be explained by discrete optically thick clouds or gas clumps crossing the line of sight, which are referred to as obscurers. These shielding gas clumps or obscurers may ensure that the radiatively driven disk winds in broad absorption line quasars are not over-ionized by UV/X-ray ionizing radiation and, rather, are accelerated further (Murray et al. 1995; Proga et al. 2000; Kaastra et al. 2014). The obscuration events may be triggered by the collapse of the BLR (Kriss et al. 2019a,b; Devereux 2021). When the continuum radiation decreases, the BLR clouds will collapse toward the accretion disk; when the continuum brightens again, these collapsed clouds might be blown away as obscurers (Kriss et al. 2019b). X-ray obscuration events also have been found in many AGN, such as NGC 5548 (Kaastra et al. 2014), NGC 3783 (Mehdipour et al. 2017; Kaastra et al. 2018; De Marco et al. 2020), NGC 985 (Ebrero et al. 2016a), and NGC 1365 (Risaliti et al. 2007; Walton et al. 2014; Rivers et al. 2015). These obscurers may be located within the BLR (Lamer et al. 2003; Risaliti et al. 2007; Lohfink et al. 2012; Longinotti et al. 2013; De Marco et al. 2020; Kara et al. 2021) or close to the outer BLR (e.g., Kaastra et al. 2014; Beuchert et al. 2015; Mehdipour et al. 2017), or near the inner torus (e.g., Beuchert et al. 2017).

Until now the relation between the WA outflows and the nuclear obscuration activity has not been fully understood. The notions of whether the WAs and obscurers have the same origin or how shielding by the obscuration affects the WAs and their appearance are not well known. Studying WAs in targets that have transient obscuration has allowed us to probe these questions. Transient obscuration events have been studied simultaneously in UV and X-rays in only a few AGN that have WAs outflows, such as NGC 5548 (Kaastra et al. 2014) and NGC 3783 (Mehdipour et al. 2017), as well as Mrk 335 (Longinotti et al. 2013; Parker et al. 2019). Studying NGC 3227 (a Seyfert 1.5 galaxy at the redshift of 0.003859<sup>1</sup>) is a rare opportunity to attempt a more general characterization. In particular, NGC 3227 was one of eight suitable targets selected for the *Neil Gehrels Swift* Observatory monitoring and triggering program (Mehdipour et al. 2017), which matches the following selection criteria: WAs in both UV and X-rays, suitably variable, bright in UV and X-rays, and adequate archival spectra for comparing with the obscured spectra. Using our target of opportunity (ToO) monitoring program of the *Neil Gehrels Swift*

Observatory, we captured another X-ray obscuration event in NGC 3227 in 2019 (Mehdipour et al. 2021, hereafter Paper I), which was observed simultaneously with *XMM-Newton*, *NuSTAR*, and *Hubble* Space Telescope/Cosmic Origins Spectrograph (HST/COS) to get a deeper multi-wavelength understanding of the transient obscuration phenomenon in AGN. The studies of WA and the obscurer are interlinked, so without having a proper model for the WA, the new obscurer cannot be accurately studied. In this work (the second paper of our series), we aim to study a comprehensive model for the WA, and then use this WA model to investigate the obscuration events appearing in NGC 3227.

It should be noted that photoionization modeling strongly depends on the ionizing spectral-energy-distribution (SED). Therefore, to properly derive the ionization structure of the WA, having an accurate broadband SED model is important. A few papers have reported studies of the WAs in NGC 3227 (Komossa & Fink 1997; Beuchert et al. 2015; Turner et al. 2018; Newman et al. 2021) and its nuclear obscurations activities (Lamer et al. 2003; Markowitz et al. 2014; Beuchert et al. 2015; Turner et al. 2018). However, the contribution of the SED components that dominate in the UV/optical band has not been adequately considered, which might affect the fitting results of the WAs and obscurers (see Paper I). The main effect of using different SEDs is that the derived ionization parameter  $\xi$  would be different. The total hydrogen column density  $N_{\text{H}}$  of the WA (i.e., sum of the individual components) would be similar, but how  $N_{\text{H}}$  is distributed over different ionization components depends on the SED. For more details, we refer to Mehdipour et al. (2016), who show the effect of using different SEDs and codes. With these considerations, we firstly built a broadband SED model from the near infrared (NIR) to hard X-rays for NGC 3227 in our Paper I. In this paper, we use this broadband SED model and a robust photoionization code (pion model; Mehdipour et al. 2016) in the SPEX package (Kaastra et al. 1996) v3.05.00 (Kaastra et al. 2020) to analyze the archival *XMM-Newton* and *NuSTAR* data taken in 2006 (Markowitz et al. 2009) and 2016 (Turner et al. 2018). Currently, SPEX is the only code that allows for the SED and the ionization balance to be fitted simultaneously, while all other codes have to pre-calculate the ionization balance on a given SED. The pion model is a self-consistent model that can simultaneously calculate the thermal/ionization balance and the plasma spectrum in the photoionization equilibrium. In this work, we focus on properties of the WAs and obscuration events of NGC 3227 with the archival 2006 and 2016 data. The detailed analysis of the 2019 obscuration events will be presented in Paper III by Mao et al. (in prep.). The discussion about how the obscurer changes over the course of the 2019 observations with the *XMM-Newton*/EPIC-pn data will be presented in Paper IV by Grafton-Waters et al. (in prep.).

This paper is organized as follows. In Sect. 2, we present the archival data that are used in this work and the data reduction process. In Sect. 3, we introduce the spectral analysis based on the broadband SED model. In Sect. 4, we present and discuss the results about WAs and obscurer components. In Sect. 5, we give a summary of our conclusions. In this work, the Cash statistic (Kaastra 2017, hereafter C-stat) will be used to estimate the goodness of fit and statistical errors will be given at  $1\sigma$  (68%) confidence level. We adopt the following flat  $\Lambda$ CDM cosmological parameters:  $H_0 = 70 \text{ km s}^{-1} \text{ Mpc}^{-1}$ ,  $\Omega_{\text{m}} = 0.30$ , and  $\Omega_{\Lambda} = 0.70$ .

<sup>1</sup> The redshift of NGC 3227 is obtained from the NASA/IPAC Extragalactic Database (NED: <https://ned.ipac.caltech.edu/>). The NED is funded by the National Aeronautics and Space Administration and operated by the California Institute of Technology.

**Table 1.** Archival *XMM-Newton* and *NuSTAR* data used for spectral analysis.

#	Observatory	ObsID	Date (yyyy-mm-dd)	Exposure (ks)
Obs1	XMM	0400270101	2006-12-03	108
Obs2	XMM	0782520201	2016-11-09	92
	<i>NuSTAR</i>	60202002002	2016-11-09	50
Obs3	XMM	0782520301	2016-11-25	74
	<i>NuSTAR</i>	60202002004	2016-11-25	43
Obs4	XMM	0782520501	2016-12-01	87
	<i>NuSTAR</i>	60202002008	2016-12-01	42
Obs5	XMM	0782520601	2016-12-05	87
	<i>NuSTAR</i>	60202002010	2016-12-05	41
Obs6	XMM	0782520701	2016-12-09	88
	<i>NuSTAR</i>	60202002012	2016-12-09	39

## 2. Observations and data reduction

In Table 1, we list the archival data used in this work. These data include six *XMM-Newton* observations (Markowitz et al. 2009; Turner et al. 2018) and five *NuSTAR* observations (Turner et al. 2018). We do not use the archival *XMM-Newton* observations taken in 2000 and on November 29, 2016 because the spectrum of the 2000 observation has a lower signal to noise ratio (S/N) owing to its short exposure time, and the observation on November 29, 2016 shows a relatively unstable softness ratio curve (see Fig. 1 of Turner et al. 2018), which may bias the estimation of WAs parameters.

### 2.1. *XMM-Newton* data

The data reduction was done using *XMM-Newton* Science Analysis Software (SAS) version 18.0.0, following the standard data analysis procedure<sup>2</sup>. The cleaned event files of EPIC-pn data were produced using the `epproc` pipeline and flaring particle background larger than 0.4 count/s was excluded. The EPIC-pn spectra and lightcurves were extracted from a circular region with a radius of 30 arcsec for the source and from a nearby source-free circular region with a radius of 35 arcsec for the background. Response matrices and ancillary response files of each observation were produced using the SAS tasks `arfgen` and `rmfgen`. Following the standard procedure, the first-order data of RGS1 and RGS2 were extracted using the SAS task `rgsproc` and flaring particle background larger than 0.2 count/s was excluded. We then combined the spectra of RGS1 and RGS2 using the SAS task `rgscombine`. We refer readers to our Paper I for the detailed data reduction of the Optical Monitor (OM) data. Only the OM UVW1 filter is available for both 2006 and 2016 observations.

### 2.2. *NuSTAR* data

For the data collected by the two *NuSTAR* telescope modules (FPMA and FPMB), level 1 calibrated and level 2 cleaned event files were produced using the standard procedure of the `nupipeline` task of HEASoft v6.27. The level 3 products – including lightcurves, spectra, and response files – were extracted using the task `nuproducts` from a circular region with a radius of 90 arcsec for the source and from a nearby source-free

circular region with the same radius for the background. Finally, we produced combined spectra of FPMA and FPMB data using the task `mathpha` and produced combined response files using the tasks `addrmf` and `addarf`.

## 3. Spectral analysis

For the 2016 archival data, we consider each set of *XMM-Newton* and *NuSTAR* observations taken on the same date as a single dataset (see Obs2 to Obs6 in Table 1), where *XMM-Newton* (OM UVW1 filter at  $\sim 2910$  Å, RGS data in the 6–37 Å wavelength range, and EPIC-pn data in the 2–10 keV energy band) and *NuSTAR* (combined FPMA and FPMB data in the 5–78 keV energy range) data are used simultaneously for the spectral analysis. For Obs1 that was taken on December 3, 2006, only the *XMM-Newton* observation is available (see Table 1), and we used Obs5 to verify that the best-fit parameters of the WAs do not significantly change without *NuSTAR* observation. In Figs. 1 and 2, we show the *XMM-Newton*/EPIC-pn light curves, softness ratio curves (the ratio of count rates between 0.3–2 and 2–10 keV bands), and the correlation between the softness ratio and 0.3–10 keV count rate for Obs1 to Obs6. According to these results, we were able to make a preliminary analysis for the state of each observation.

**Obs1.** This observation was considered to be in an unobscured state by Markowitz et al. (2009). However, compared with the average softness ratio of the six observations (see the dashed red line in the bottom panel of Fig. 1), a significant spectral hardening (softness ratio below the average value) occurred in the beginning of this observation (see the bottom panel of the first column in Fig. 1), which might indicate the existence of an obscuration event. After this spectral hardening period, the softness ratio of Obs1 returns to the average value, which might indicate that this obscuration event has disappeared. These phenomena mean that these two periods of Obs1 should be analyzed separately. According to the difference between the softness ratio of Obs1 and the average softness ratio of the six observations, Obs1 is subdivided into the following two slices: S1a and S1b (see the first column in Fig. 1). S1b is consistent with being in an unobscured state as it follows the correlation of Obs2 to Obs5 (see the right panel of Fig. 2). However, S1a has a harder spectrum that is similar to S6a and S6b (see the right panel of Fig. 2), and it might be in an obscured state (however, this was not reported in previous works).

**Obs2 to Obs5.** According to Turner et al. (2018), Obs2 to Obs5 are in unobscured states, which show a linear correlation between the softness ratio (0.3–1/1–10 keV) and 0.3–10 keV count rate. We confirm this linear correlation for these observations (softness ratio is calculated between the 0.3–2 and 2–10 keV bands in this work) in the left panel of Fig. 2. It is worth noting that although Obs2 and Obs3 show a spectral hardening during some periods, these periods still follow the correlation of unobscured states (see the left panel of Fig. 2). Therefore, these periods might not be in obscured states.

**Obs6.** Turner et al. (2018) had observed a rapid obscuration event in Obs6. To restudy this obscuration event using a broadband SED model and the `pion` model in SPEX, we followed Turner et al. (2018) to subdivide Obs6 into three slices: S6a, S6b, and S6c (see Fig. 1). S6c shows an unobscured state as it follows the correlation of Obs2 to Obs5 (see the right panel of Fig. 2). However, S6a and S6b deviate from the correlation of Obs2 to Obs5 (see the right panel of Fig. 2); therefore, they might reside in obscured states.

<sup>2</sup> See <https://www.cosmos.esa.int/web/xmm-newton/sas-threads> for details.



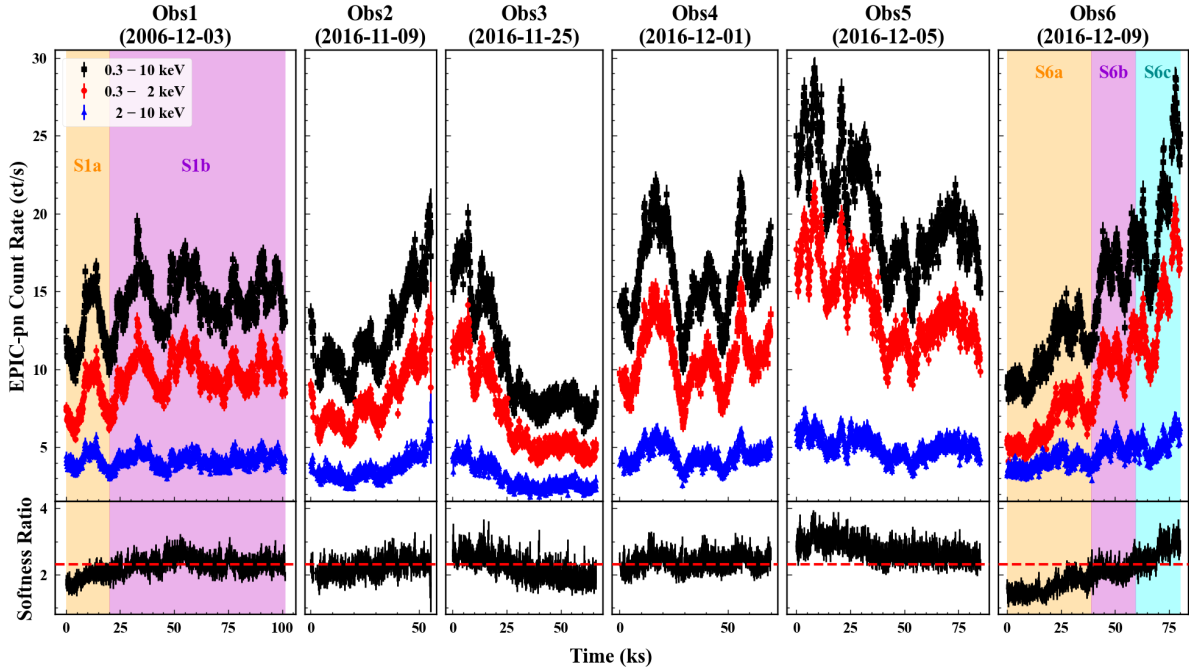


**Fig. 1.** *XMM-Newton*/EPIC-pn light curves (red points: 0.3–2 keV; blue points: 2–10 keV; black points: 0.3–10 keV) of NGC 3227 (*top panel*) and softness ratio curves between the count rates in 0.3–2 keV and 2–10 keV bands ( $\text{Soft}_{0.3-2\text{keV}}/\text{Hard}_{2-10\text{keV}}$ ; *bottom panel*) with the time bin of 100 s. The red horizontal dashed line in the *bottom panel* is the average softness ratio of all the six observations. According to the difference between the softness ratio of each observation (black points in the *bottom panel*) and the average softness ratio (horizontal dashed line in red), Obs1 is divided into two slices that are S1a (orange region of the first column) and S1b (violet region of the first column), and Obs6 is divided into three slices that are S6a (orange region of the last column), S6b (violet region of the last column), and S6c (cyan region of the last column).

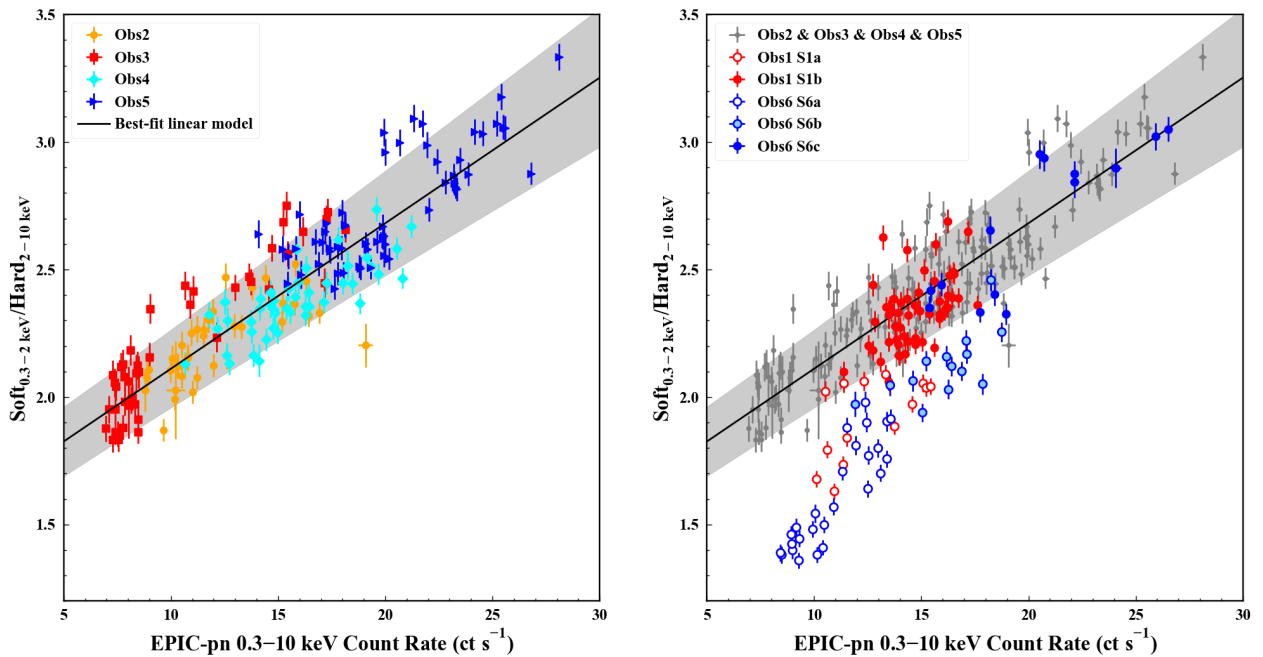


**Fig. 2.** Correlation between the softness ratio (the ratio of count rates between 0.3–2 and 2–10 keV bands), and 0.3–10 keV count rate, for Obs2 to Obs5 (*left panel*), and for Obs1 and Obs6 (*right panel*). In both *left* and *right panels*, the black solid line is the best-fit linear model of  $y = (0.06 \pm 0.01)x + (1.54 \pm 0.13)$  for Obs2 to Obs5. The shaded grey region is the associated  $1\sigma$  uncertainty.

Next, we carried out a detailed spectral analysis for these observational data. We began our spectral modeling by using a broadband SED model from the NIR to the hard X-ray bands for NGC 3227. We refer to our Paper I for the full details on this SED model and we only give a brief introduction here.

The main spectral components that are used in this work are as follows.

1. The intrinsic broadband SED (see details in Paper I), which is composed of a disk blackbody component (dbb), a warm Comptonized disk component (comt) from the optical to

**Table 2.** Best-fit parameters of the intrinsic broadband SED.

Comp.	Parameter	Obs1	Obs2	Obs3	Obs4	Obs5	Obs6
dbb	Normalization $A$ ( $10^{26}$ cm $^2$ )	5.87 (s)	7.51 (s)	7.15 (s)	6.87 (s)	7.27 (s)	7.39 (s)
comt	Normalization ( $10^{54}$ ph s $^{-1}$ keV $^{-1}$ )	$1.70^{+0.24}_{-0.20}$	$1.00^{+0.21}_{-0.25}$	$0.50 \pm 0.15$	$1.61^{+0.30}_{-0.27}$	$1.06^{+0.05}_{-0.16}$	$1.65^{+3.74}_{-0.19}$
pow	Normalization ( $10^{50}$ ph s $^{-1}$ keV $^{-1}$ )	$4.02 \pm 0.06$	$2.93 \pm 0.06$	$2.25 \pm 0.04$	$3.60 \pm 0.06$	$4.64^{+0.07}_{-0.01}$	$4.59^{+0.25}_{-0.10}$
	Photon index $\Gamma$	$1.81 \pm 0.01$	$1.73 \pm 0.02$	$1.66 \pm 0.01$	$1.78 \pm 0.009$	$1.88 \pm 0.01$	$1.86 \pm 0.03$
refl	Incident power-law normalization	4.02 (c)	2.93 (c)	2.25 (c)	3.60 (c)	4.64 (c)	4.59 (c)
	Incident power-law photon index	1.81 (c)	1.73 (c)	1.66 (c)	1.78 (c)	1.88 (c)	1.86 (c)
	Reflection scale $s$	$0.67 \pm 0.04$	$0.54 \pm 0.07$	$0.30 \pm 0.03$	$0.42 \pm 0.03$	$0.68 \pm 0.011$	$0.57 \pm 0.05$
Luminosity ( $10^{42}$ erg s $^{-1}$ )	0.3–2 keV luminosity $L_{0.3-2\text{keV}}$	1.28	0.90	0.66	1.14	1.42	1.48
	2–10 keV luminosity $L_{2-10\text{keV}}$	1.45	1.20	1.00	1.32	1.50	1.54
	1–1000 Ryd ionizing luminosity $L_{\text{ion}}$	19.1	17.8	14.6	19.8	19.2	23.5
	Bolometric luminosity $L_{\text{bol}}$	43.3	47.1	42.4	46.6	47.1	52.2
$C$ -stat/ $C$ -expt. (Best-fit)	(SED+WAs)	3439/2794 (S1b)*	4456/3621*	3834/3584	4105/3588	4121/3570	3762/3638 (S6c)
	(SED+OC $_L$ +WAs)	3261/2926 (S1a)					3819/3670 (S6b)
	(SED+OC $_H$ +OC $_L$ +WAs)						3786/3654 (S6a)

**Notes.** The disk blackbody component (dbb) normalization followed by “(s)” is obtained by scaling the dbb normalization of the 2019 observation (see Paper I) to match the OM UVW1 flux of each archival observation. Given that the spectral shape of the emission from the outer disc might not have a strong variability on short timescales, for simplicity, the following parameters are fixed to those of the 2019 observation: the dbb maximum temperature  $T_{\text{max}} = 10$  eV, the warm Comptonized disk component (comt) seed photon temperature  $T_{\text{seed}} = 10$  eV, the comt electron temperature  $T_e = 60$  eV, and the comt optical depth  $\tau = 30$ . The normalization of the neutral reflection component (refl) denoted by “(c)” is coupled to the normalization of the X-ray power-law component (pow) in the fit, and the photon index ( $\Gamma$ ) of the refl denoted by “(c)” is coupled to the photon index of the pow. The 0.3–2 keV luminosity ( $L_{0.3-2\text{keV}}$ ), 2–10 keV luminosity ( $L_{2-10\text{keV}}$ ), 1–1000 Ryd ionizing luminosity ( $L_{\text{ion}}$ ), and bolometric luminosity ( $L_{\text{bol}}$ ) present the intrinsic luminosities. The  $C$ -stat is the  $C$ -statistic value of the final fitting result corresponding to the best-fit model and the  $C$ -expt. is the expected  $C$ -stat. The best-fit model is shown as follows: for Obs1 S1b, Obs2, Obs3, Obs4, Obs5, or Obs6 S6c, it is the intrinsic SED plus the four warm absorbers (WAs), i.e., SED+WAs; for Obs S1a or Obs6 S6b, it is the intrinsic SED plus one low-ionization obscurer component (OC $_L$ ) plus the four WAs, i.e., SED+OC $_L$ +WAs; for Obs6 S6a, it is the intrinsic SED plus one high-ionization obscurer component (OC $_H$ ) plus OC $_L$  plus the four WAs, i.e., SED+OC $_H$ +OC $_L$ +WAs. The best-fit SED parameters of Obs1 is obtained by fitting the spectra of S1b, and the best-fit SED parameters of Obs6 is obtained by fitting the spectra of S6c. The SED parameters of S1a are fixed to those of S1b; the parameters of both S6a and S6b are fixed to those of S6c. Compared with other observations or slices, Obs1 S1b and Obs2 have relatively worse fitting results that are denoted by “\*”, which are mainly due to the uncertainties in the intercalibration between *XMM-Newton* and *NuSTAR*.

the soft X-ray band, an X-ray power-law component (pow), and a neutral reflection component (refl) in the hard X-ray energy band. For the pow of NGC 3227, we used 309 keV (Turner et al. 2018) as the high-energy exponential cut-off and 13.6 eV as the low-energy exponential cut-off.

2. The obscurer components, which heavily absorb the X-ray spectrum. We used the pion model in SPEX to fit their absorption features in the spectrum.

3. The warm absorber (WA) components, which produce absorption features in soft X-rays. We also used the pion model to fit these absorption features.

4. The Galactic X-ray absorption, which was taken into account by the hot model in SPEX with the hydrogen column density  $N_{\text{H}} = 2.07 \times 10^{20}$  cm $^{-2}$  (Murphy et al. 1996).

Obs2 to Obs5, S1b, and S6c are in unobscured states, so we will fit their spectra using the spectral components 1, 3, and 4. S1a, S6a, and S6b are in obscured states, so their spectra will be fitted with spectral components 1–4. In the next subsection, we present the details of the spectral analysis for spectral components 1, 2, and 3.

### 3.1. The intrinsic broadband SED

For the archival data, only the OM UVW1 filter data is available for all the six observations, so the parameters of the dbb component might not be well constrained for the fit. Moreover, we do not expect a strong variability in the shape of the emission from the outer disc on short timescales. It is also common for the variability of the flux in long wavelengths to be significantly smaller than that of the X-ray band. Therefore, we assume

that the shape of the dbb component of each archival observation is similar to that of the 2019 observation which has optical and UV observational data to constrain the dbb component (see Paper I); that is to say, we fixed the maximum temperature  $T_{\text{max}}$  of the dbb component of the archival data to the 10 eV of the 2019 observation (see Paper I) and scaled the dbb normalization of the archival observations according to the normalization of the 2019 observation (the scale factor of each archival observation is the OM UVW1 flux ratio between the 2019 observation and each archival observation). For the comt component, its normalization was free in the fit and the following parameters were fixed to those of the 2019 observation (see details in Paper I): seed photon temperature  $T_{\text{seed}} = 10$  eV, electron temperature  $T_e = 60$  eV, and optical depth  $\tau = 30$ . The dbb and comt components mainly dominate in the energy band below 0.5 keV (see Paper I), so fixing the shapes of these two components might bring uncertainties to the parameter estimates for the WAs. Even so, the normalizations of these two components, which are free in the fits, are still the main factors to affect the fitting result. For each slice in an obscured state (S1a, S6a, and S6b), we assumed that it has the same intrinsic broadband SED as the unobscured slice in the same observation (S1b, S6c, and S6c, respectively). Therefore, we fixed the parameters of dbb, comt, pow, and refl components of S1a to those of S1b in the fit. Similarly, these parameters of S6a and S6b were fixed to those of S6c. For the refl component, the scaling factor of the reflected spectrum ( $s$ ) was free in the fit, the incident power-law normalization and photon index were coupled to those of the pow component. We summarize the best-fit parameters of the intrinsic broadband SED in Table 2 (discussed in Sect. 4.1).

**Table 3.** Best-fit parameters of the four WAs (WA<sub>1</sub>, WA<sub>2</sub>, WA<sub>3</sub>, WA<sub>4</sub>) for Obs1 to Obs6: hydrogen column density ( $N_{\text{H}}$ ), ionization parameter ( $\xi$ ), outflow velocity ( $v_{\text{out}}$ ), and turbulent velocity ( $\sigma_v$ ).

Component	Parameter	03 Dec. 2006		09 Nov. 2016	25 Nov. 2016	01 Dec. 2016	05 Dec. 2016	09 Dec. 2016		
		Obs1		Obs2	Obs3	Obs4	Obs5	S6c	S6b*	S6a*
WA <sub>1</sub>	$N_{\text{H}}$ ( $10^{22}$ cm <sup>-2</sup> )	2.27 (f)	2.27 (f)	2.27 (f)	2.27 (f)	2.27 (f)	2.27 <sup>+0.08</sup> <sub>-0.19</sub>	2.27 (f)	2.27 (f)	2.27 (f)
	$\log [\xi]$ (erg cm s <sup>-1</sup> )	2.96 ± 0.04	2.93	2.92 ± 0.04	3.21 ± 0.06	3.29 ± 0.05	3.29 <sup>+0.08</sup> <sub>-0.04</sub>	3.04 <sup>+0.24</sup> <sub>-0.06</sub>	3.02	2.94
	$v_{\text{out}}$ (km s <sup>-1</sup> )	-1270 (f)	-1270 (f)	-1270 (f)	-1270 (f)	-1270 (f)	-1270 <sup>+20</sup> <sub>-120</sub>	-1270 (f)	-1270 (f)	-1270 (f)
	$\sigma_v$ (km s <sup>-1</sup> )	20 (f)	20 (f)	20 (f)	20 (f)	20 (f)	20 <sup>+20</sup> <sub>-10</sub>	20 (f)	20 (f)	20 (f)
WA <sub>2</sub>	$N_{\text{H}}$ ( $10^{22}$ cm <sup>-2</sup> )	0.25 (f)	0.25 (f)	0.25 (f)	0.25 (f)	0.25 (f)	0.25 ± 0.04	0.25 (f)	0.25 (f)	0.25 (f)
	$\log [\xi]$ (erg cm s <sup>-1</sup> )	2.54 ± 0.02	2.51	2.68 ± 0.03	2.74 ± 0.04	2.65 ± 0.03	2.59 ± 0.02	2.58 <sup>+0.21</sup> <sub>-0.03</sub>	2.56	2.47
	$v_{\text{out}}$ (km s <sup>-1</sup> )	-500 (f)	-500 (f)	-500 (f)	-500 (f)	-500 (f)	-500 <sup>+60</sup> <sub>-50</sub>	-500 (f)	-500 (f)	-500 (f)
	$\sigma_v$ (km s <sup>-1</sup> )	140 (f)	140 (f)	140 (f)	140 (f)	140 (f)	140 <sup>+10</sup> <sub>-20</sub>	140 (f)	140 (f)	140 (f)
WA <sub>3</sub>	$N_{\text{H}}$ ( $10^{22}$ cm <sup>-2</sup> )	0.12 (f)	0.12 (f)	0.12 (f)	0.12 (f)	0.12 (f)	0.12 ± 0.012	0.12 (f)	0.12 (f)	0.12 (f)
	$\log [\xi]$ (erg cm s <sup>-1</sup> )	1.91 ± 0.07	1.88	2.22 ± 0.09	2.55 ± 0.13	1.84 ± 0.08	1.89 ± 0.07	1.97 <sup>+0.19</sup> <sub>-0.15</sub>	1.94	1.86
	$v_{\text{out}}$ (km s <sup>-1</sup> )	-440 (f)	-440 (f)	-440 (f)	-440 (f)	-440 (f)	-440 <sup>+160</sup> <sub>-80</sub>	-440 (f)	-440 (f)	-440 (f)
	$\sigma_v$ (km s <sup>-1</sup> )	50 (f)	50 (f)	50 (f)	50 (f)	50 (f)	50 ± 20	50 (f)	50 (f)	50 (f)
WA <sub>4</sub>	$N_{\text{H}}$ ( $10^{22}$ cm <sup>-2</sup> )	0.16 (f)	0.16 (f)	0.16 (f)	0.16 (f)	0.16 (f)	0.16 ± 0.007	0.16 (f)	0.16 (f)	0.16 (f)
	$\log [\xi]$ (erg cm s <sup>-1</sup> )	-1.25 ± 0.11	-1.28	-1.13 <sup>+0.20</sup> <sub>-0.16</sub>	-0.69 <sup>+0.17</sup> <sub>-0.20</sub>	-1.40 ± 0.16	-1.06 ± 0.11	-1.23 <sup>+0.12</sup> <sub>-0.98</sub>	-1.25	-1.28
	$v_{\text{out}}$ (km s <sup>-1</sup> )	-110 (f)	-110 (f)	-110 (f)	-110 (f)	-110 (f)	-110 <sup>+90</sup> <sub>-30</sub>	-110 (f)	-110 (f)	-110 (f)
	$\sigma_v$ (km s <sup>-1</sup> )	260 (f)	260 (f)	260 (f)	260 (f)	260 (f)	260 <sup>+40</sup> <sub>-30</sub>	260 (f)	260 (f)	260 (f)

**Notes.** The parameters followed by “(f)” are fixed to the value of Obs5 that has the highest S/N. The slices denoted by “\*” mean that they are in obscured states.

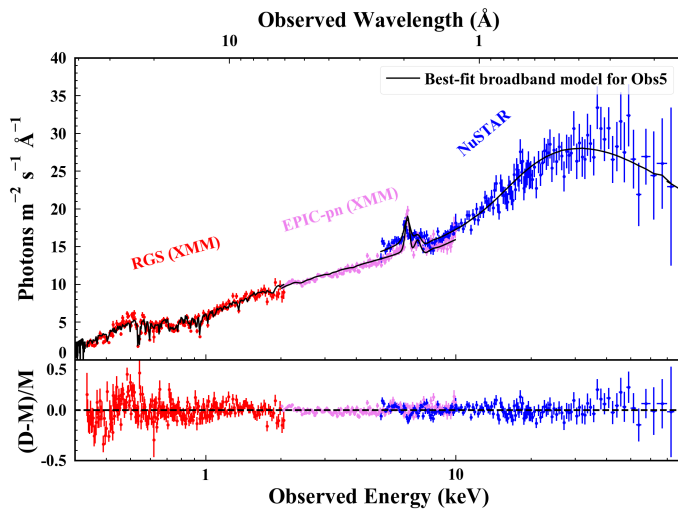


**Fig. 3.** Observational data (colored data points) with the best-fit broadband SED model in the X-ray band (black solid curve) for Obs5 (*top panel*). Residuals of the best-fit model (“D” is the observational data and “M” is the best-fit model) for Obs5 (*bottom panel*). Obs5 is given as an example (other observations have similar fitting results).

### 3.2. Warm absorber components

The hydrogen column density ( $N_{\text{H}}$ ), outflow velocity ( $v_{\text{out}}$ ), and turbulent velocity ( $\sigma_v$ ) of the WAs are not well constrained simultaneously for the spectrum with low S/N and these parameters might not vary significantly between different observations. Therefore, we fixed these parameters of Obs1–Obs4 and Obs6 to the best-fit results of Obs5 (see Table 3), because Obs5 has the highest S/N. Therefore, for Obs1–Obs4 and Obs6, only  $\xi$  was free in the fit (see Table 3). Actually,  $N_{\text{H}}$ ,  $v_{\text{out}}$ , and  $\sigma_v$  are not expected to be constant, so our assumption will bring extra uncertainties to the parameter estimates. However,  $N_{\text{H}}$ ,  $v_{\text{out}}$ , and  $\sigma_v$  might not vary significantly on short timescales compared with  $\xi$ , so a significant impact on the fitting results with these parameters fixed might not be expected. For simplicity, we assumed that the WAs fully cover the X-ray source (covering

factor  $C_f = 1$ ) and have solar abundances (Lodders et al. 2009). The best-fit results of the WAs are discussed in Sect. 4.2.

### 3.3. Obscured components

Parameters  $v_{\text{out}}$  and  $\sigma_v$  of the obscured components were difficult to constrain owing to the lack of well defined and strong absorption lines. We verified that changing their values had little impact on other parameters. Therefore, we fixed  $v_{\text{out}}$  and  $\sigma_v$  of the obscured components to their default values ( $v_{\text{out}} = 0$  km s<sup>-1</sup> and  $\sigma_v = 100$  km s<sup>-1</sup>). With that, the obscured components,  $N_{\text{H}}$ ,  $\xi$ , and  $C_f$  are free in the fit. We will discuss the best-fit results of obscured components in Sect. 4.3.

## 4. Results and discussion

### 4.1. Intrinsic broadband SED

The broadband SED model provides a good description for the observational data (see Table 2 and Fig. 3, where Obs5 is given as an example). Compared with other observations or slices, Obs1 S1b and Obs2 have relatively worse fitting results (see Table 3); this is mainly due to the uncertainties in the intercalibration between *XMM-Newton* and *NuSTAR*. The intrinsic unabsorbed broadband SEDs of Obs1 to Obs6 are shown in Fig. 4 and their best-fit parameters are listed in Table 2. The intrinsic broadband SED of NGC 3227 shows a significant variability at energies  $\geq 0.03$  keV, especially in the X-ray band (see Fig. 4). According to the Spearman rank method, there is a positive correlation between the photon index of the pow ( $\Gamma$ ; see Table 2) and the intrinsic 2–10 keV luminosity ( $L_{2-10\text{keV}}$ ; see Table 2), where the correlation coefficients  $r_s = 0.94$  and the associated  $p$ -values  $p_s = 0.005$ , showing a “softer-when-brighter” behavior. This behavior has been observed in many Seyfert galaxies (e.g., Markowitz & Edelson 2004; Ponti et al. 2006; Sobolewska & Papadakis 2009; Soldi et al. 2014). Peretz & Behar (2018) also found a softer-when-brighter variability behavior in NGC 3227, which might be driven by varying absorption rather than by the intrinsic variability of the central source. The averaged ionizing luminosity over 1–1000 Ryd is around  $1.9 \times 10^{43}$  erg s<sup>-1</sup>

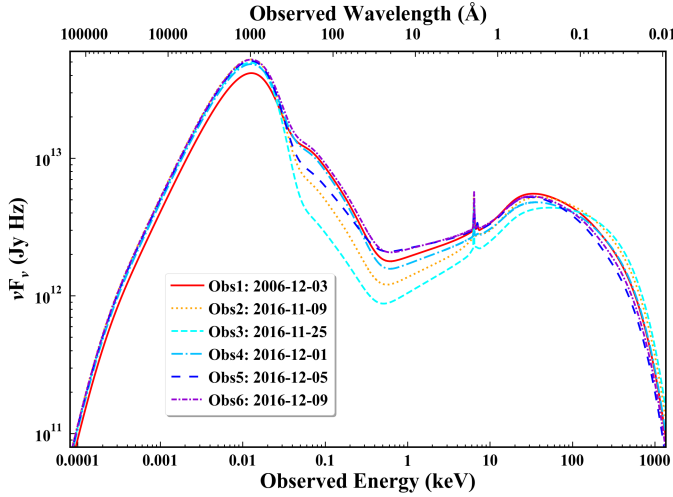


Fig. 4. Intrinsic unabsorbed broadband SEDs of Obs1–Obs6.

(see Table 2), which is two times larger than the results of [Beuchert et al. \(2015\)](#) and [Turner et al. \(2018\)](#). This might be due to the different SED model in the UV and soft X-ray bands. The averaged full-band bolometric luminosity ( $L_{\text{bol}}$ ) is about  $4.6 \times 10^{43} \text{ erg s}^{-1}$  (see Table 2), which is 1.5 times smaller than the result of [Woo & Urry \(2002\)](#) based on the flux integration method. According to the reverberation mapping method, the black hole mass ( $M_{\text{BH}}$ ) of NGC 3227 is  $5.96 \times 10^6 M_{\odot}$  for NGC 3227 ([Bentz & Katz 2015](#)). The Eddington luminosity ( $L_{\text{Edd}}$ ) of NGC 3227 is  $7.45 \times 10^{44} \text{ erg s}^{-1}$ , which is calculated by  $L_{\text{Edd}} = 1.25 \times 10^{38} \times (M_{\text{BH}}/M_{\odot})$  ([Rybicki & Lightman 1979](#)). Therefore, the averaged Eddington ratio of NGC 3227 is about 6%.

#### 4.2. Warm absorber components

At least four WA components (see Table 3) were required to improve the fitting result ( $\Delta C \sim 100$  for adding  $\text{WA}_1$ ,  $\Delta C \sim 80$  for adding  $\text{WA}_2$ ,  $\Delta C \sim 80$  for adding  $\text{WA}_3$ ,  $\Delta C \sim 500$  for adding  $\text{WA}_4$ ). We added another component (a fifth component), but it did not improve the fitting result ( $\Delta C \sim 2$ ). Our result is not consistent with that in [Turner et al. \(2018\)](#), which detected three WA components. This might be due to the different SED model and photoionization models between our respective works. The best-fit model shows some weak residual emission features in the 0.5–0.6 keV band (see Fig. 3) caused by the oxygen line emission from distant regions, similarly to NGC 5548 ([Mao et al. 2018](#)). The quality of our spectrum is not equipped for a detailed modeling of these emission lines, and they are too weak to affect our modeling of the absorbing wind components. Thus, we do not discuss them further.

##### 4.2.1. Parameters of the warm absorbers

The logarithm of the ionization parameter (in units of  $\text{erg cm s}^{-1}$ ) for each WA component is around 3.0 for  $\text{WA}_1$ , 2.5 for  $\text{WA}_2$ , 2.0 for  $\text{WA}_3$ , and  $-1.0$  for  $\text{WA}_4$  (see Table 3).  $\text{WA}_2$ ,  $\text{WA}_3$ , and  $\text{WA}_4$  have a similar column density around  $10^{21} \text{ cm}^{-2}$ , while  $\text{WA}_1$  has a much higher value near  $10^{22} \text{ cm}^{-2}$  (see Table 3). In Paper I, we adopt a de-ionization scenario for the WAs and simultaneously fitted the spectra of the archival unobserved observation taken on December 5, 2016 and the new obscured observations taken in

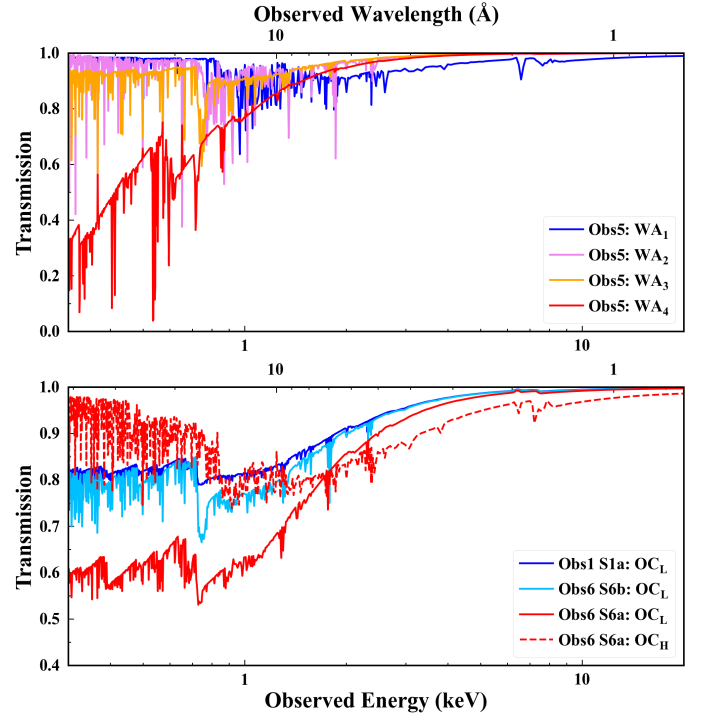


Fig. 5. Transmission spectra of the four WAs of Obs5 ( $\text{WA}_1$ ,  $\text{WA}_2$ ,  $\text{WA}_3$ ,  $\text{WA}_4$  (top panel; Obs5 is given as an example) and obscurer components of S6a, S6b, and S1a (bottom panel).  $\text{OC}_L$  is the low-ionization obscurer component, while  $\text{OC}_H$  is the high-ionization obscurer component.

2019. In this work, we fit the spectra taken on 2016 December 05 alone. Therefore, some different results between Paper I and Paper II can be expected because of the differences in the spectral modeling. The X-ray transmission of each WA component in our line of sight to the central region is shown in the top panel of Fig. 5. We can see that  $\text{WA}_1$  mainly absorbs the continuum radiation between 0.8 and 10 keV. Furthermore,  $\text{WA}_2$  and  $\text{WA}_3$  produce absorption features between 0.7 and 5 keV, whereas  $\text{WA}_4$  heavily absorbs the continuum below 5 keV. From  $\text{WA}_1$  to  $\text{WA}_4$ , the outflow velocity gradually decreases from  $\sim 1300$  to  $\sim 100 \text{ km s}^{-1}$  (see Table 3), which shows a positive correlation with the ionization parameter. This correlation is consistent with the results for AGN samples ([Tombsi et al. 2013](#); [Laha et al. 2014](#)). These previous studies indicated that this correlation cannot be explained by the radiatively driven or magneto hydrodynamically driven outflowing mechanism ([Tombsi et al. 2013](#); [Laha et al. 2014](#)), and it might be explained by the equilibrium between the radiation pressure on WAs and the drag pressure from the ambient circumnuclear medium (see details in Wang et al., in prep.).

##### 4.2.2. Radial location of the warm absorbers

We used three methods to estimate the upper or lower limit of the locations of the various WA components. First, we assumed that the thickness ( $\Delta r$ ) of the WA cloud does not exceed its distance ( $r$ ) to the SMBH ([Krolik & Kriss 2001](#); [Blustin et al. 2005](#)). As  $N_{\text{H}} \approx n_{\text{H}} C_{\text{v}} \Delta r$ , so the upper limit of the distance  $r_{\text{max}} \approx \Delta r \approx N_{\text{H}} / (n_{\text{H}} C_{\text{v}})$ , where  $C_{\text{v}}$  is the volume filling factor. Combined with Eq. (1),  $r_{\text{max}}$  can be estimated by

$$r_{\text{max}} = \frac{L_{\text{ion}} C_{\text{v}}}{\xi N_{\text{H}}} \quad (2)$$



Assuming that the total outflow momentum of the WA cloud is equal to the momentum of the absorbed radiation ( $P_{\text{abs}}$ ) plus the momentum of the ionizing luminosity being scattered ( $P_{\text{scat}}$ ),  $C_v$  can be calculated as follows (Blustin et al. 2005; Grafton-Waters et al. 2020):

$$C_v = \frac{(\dot{P}_{\text{abs}} + \dot{P}_{\text{scat}})\xi}{1.23m_p L_{\text{ion}} v_{\text{out}}^2 \Omega}. \quad (3)$$

Here,  $\dot{P}_{\text{abs}}$  is given by

$$\dot{P}_{\text{abs}} = \frac{L_{\text{abs}}}{c}, \quad (4)$$

where  $L_{\text{abs}}$  is the absorbed luminosity, and  $\dot{P}_{\text{scat}}$  is calculated by

$$\dot{P}_{\text{scat}} = \frac{L_{\text{ion}}}{c}(1 - e^{-\tau_T}); \tau_T = \sigma_T N_H, \quad (5)$$

where  $\tau_T$  is the optical depth for Thomson scattering, and  $\sigma_T$  is the Thomson scattering cross-section. We use the ionizing luminosity of Obs5 to estimate the distance as the WAs parameters are mainly from the spectral fitting of Obs5. The estimated upper limit ( $r_{\text{max}}$  in Eq. (2)) of the radial location of each WA component is summarized in Table 4, which is 0.007 pc for WA<sub>1</sub>, 0.24 pc for WA<sub>2</sub>, 0.71 pc for WA<sub>3</sub>, and 265 pc for WA<sub>4</sub>.

The second method is based on the assumption that the outflow velocities of winds are larger than or equal to their escape velocities  $v_{\text{esc}} = \sqrt{2GM_{\text{BH}}/r}$  (Blustin et al. 2005), then we can obtain the lower limit of  $r$  via:

$$r_{\text{min}} = \frac{2GM_{\text{BH}}}{v_{\text{out}}^2}, \quad (6)$$

where  $G$  is the gravitational constant. The lower limit of the radial location of each WA component is estimated to be 0.03 pc for WA<sub>1</sub>, 0.2 pc for WA<sub>2</sub>, 0.3 pc for WA<sub>3</sub>, and 4 pc for WA<sub>4</sub> (see Table 4).

The third method for estimating the radial location of WAs is based on the recombination timescale. Following Bottorff et al. (2000), the recombination timescale of the ion  $X_i$  is defined as

$$t_{\text{rec}}(X_i) = \left( \alpha_r(X_i) n_e \left[ \frac{f(X_{i+1})}{f(X_i)} - \frac{\alpha_r(X_{i-1})}{\alpha_r(X_i)} \right] \right)^{-1}, \quad (7)$$

where  $\alpha_r(X_i)$  is the recombination coefficient (recombination rate from the ion  $X_{i+1}$  to  $X_i$ ),  $n_e$  is the electron number density of the absorbing gas, and  $f(X_i)$  is the fraction of ion  $X_i$ . We select the ions that contribute significantly to the spectral fit for each WA component as the indicators of this component. Some of these parameters can be obtained from SPEX code (Mao & Kaastra 2016):  $\alpha_r(X_i)$  and  $\alpha_r(X_{i-1})$  come from atomic physics, and  $f(X_i)$  and  $f(X_{i+1})$  are estimated from the ionization balance. Then we can obtain  $nt_{\text{rec}}$  (see Table 4). The  $t_{\text{rec}}$  of each WA component can be estimated by the variation timescale of the ionization parameters between different observations (e.g., Ebrero et al. 2016b). For WA<sub>1</sub>, the ionization parameter shows a significant variation between Obs2 and Obs3, so its  $t_{\text{rec}}$  might be lower than the time interval between Obs2 and Obs3 (16 days). For WA<sub>2</sub>, there is a significant change for the ionization parameter between Obs3 and Obs5, so its  $t_{\text{rec}}$  might be smaller than the time interval between Obs3 and Obs5 (10 days). For both WA<sub>3</sub> and WA<sub>4</sub>, Obs3, and Obs4 have a significantly different ionization parameter, which indicates that their values for  $t_{\text{rec}}$  might be smaller than the time interval between Obs3 and Obs4 (6 days). However, we cannot make a clear conclusion about the

**Table 4.** Estimated distances ( $r$ ) of the four WAs (WA<sub>1</sub>, WA<sub>2</sub>, WA<sub>3</sub>, and WA<sub>4</sub>) of NGC 3227.

Parameter	WA <sub>1</sub>	WA <sub>2</sub>	WA <sub>3</sub>	WA <sub>4</sub>
Method 1 (*): Distance $r \geq$ thickness $\Delta r$				
$\dot{P}_{\text{abs}}$ ( $10^{33}$ erg m <sup>-1</sup> ) <sup>(a)</sup>	1.68	1.44	1.54	51.3
$\dot{P}_{\text{scat}}$ ( $10^{32}$ erg m <sup>-1</sup> ) <sup>(b)</sup>	9.6	1.1	0.5	0.7
$C_v$ <sup>(c)</sup>	0.049	0.039	0.011	0.006
$r$ (pc) <sup>(d)</sup>	$\leq 0.007$	$\leq 0.24$	$\leq 0.71$	$\leq 265$
Method 2 (†): Outflow velocity $v_{\text{out}} \geq$ escape velocity $v_{\text{esc}}$				
$r$ (pc) <sup>(e)</sup>	$\geq 0.03$	$\geq 0.2$	$\geq 0.3$	$\geq 4$
Method 3 (‡): Recombination timescale method				
$\langle n_e t_{\text{rec}} \rangle$ ( $10^{10}$ s cm <sup>-3</sup> )	5.6	5.4	3.9	7.2
$t_{\text{rec}}$ (days) <sup>(f)</sup>	$\leq 16$	$\leq 10$	$\leq 6$	$\leq 6$
$\langle n_e \rangle$ ( $10^{10}$ cm <sup>-3</sup> ) <sup>(g)</sup>	$\geq 4.0$	$\geq 6.3$	$\geq 7.5$	$\geq 14.0$
$r$ (pc) <sup>(h)</sup>	$\leq 0.16$	$\leq 0.3$	$\leq 0.6$	$\leq 13$

**Notes.** (\*) First method for estimating the distances of the WAs, based on the assumption that the thickness ( $\Delta r$ ) of the WA cloud does not exceed its distance ( $r$ ) (see Eqs. (2)–(5)).<sup>(a)</sup> Momentum outflow rate from the radiation being absorbed. <sup>(b)</sup> Momentum outflow rate from the radiation being scattered. <sup>(c)</sup> Volume filling factor. <sup>(d)</sup> The distances of the WAs that are estimated by the first method. <sup>(e)</sup> The second method to estimate the distances of the WAs, which is based on the assumption that the outflow velocities of winds ( $v_{\text{out}}$ ) are larger than or equal to their escape velocities ( $v_{\text{esc}}$ ) (see Eq. (6)). <sup>(f)</sup> Distances of the WAs that are estimated by the second method. <sup>(g)</sup> Third method to estimate the distances of the WAs, which is based on the recombination timescale (see Eq. (7)). <sup>(h)</sup> Recombination time scale. <sup>(i)</sup> Electron number density. <sup>(j)</sup> Distances of the WAs that are estimated by the third method.

lower limits of the  $t_{\text{rec}}$  for these WA components because of the low number of observations. We list the  $t_{\text{rec}}$  of each WA component in Table 4. According to  $t_{\text{rec}}$ ,  $nt_{\text{rec}}$ , and Eq. (1) (we also use the ionizing luminosity of Obs5 here), the radial distance is estimated to be  $\leq 0.16$  pc for WA<sub>1</sub>,  $\leq 0.3$  pc for WA<sub>2</sub>,  $\leq 0.6$  pc for WA<sub>3</sub>,  $\leq 13$  pc for WA<sub>4</sub> (see Table 4). These estimates are consistent with the results obtained by Eqs. (2) and (6) (see Table 4 and Fig. 6).

The radial location of the optical BLR of NGC 3227 is estimated to be around 0.0032 pc from the time lag between the H $\beta$  line and continuum at 5100 Å (Denney et al. 2009). The optical [O III]  $\lambda 5007$  image indicates that the narrow line region (NLR) of NGC 3227 can extend to  $\sim 100$  pc (Schmitt & Kinney 1996), even to  $\sim 500$  pc (Mundell et al. 1995). According to Nenkova et al. (2008a), the inner radius of the torus can be estimated by

$$R_{\text{in}} = 0.4 \times \left( \frac{L_{\text{bol}}}{10^{45} \text{ erg s}^{-1}} \right)^{0.5} \left( \frac{1500 \text{ K}}{T_d} \right)^{2.6} \text{ pc}, \quad (8)$$

with a dust temperature of  $T_d = 1500$  K. If  $L_{\text{bol}} = 4.6 \times 10^{43}$  erg s<sup>-1</sup> (see Sect. 4.1),  $R_{\text{in}}$  is about 0.09 pc. The outer radius can be estimated by  $R_{\text{out}} = Y \times R_{\text{in}}$ . Using the clumpy model (Nenkova et al. 2002, 2008a,b), Alonso-Herrero et al. (2011) estimated that the  $Y$  of NGC 3227 is about 17, so  $R_{\text{out}}$  is around 1.46 pc. The distance estimates for the BLR, torus, NLR, and each WA component of NGC 3227 are shown in Fig. 6.

As Fig. 6 shows, WA<sub>1</sub> lies between the outer region of the BLR and the inner region of torus; WA<sub>2</sub> and WA<sub>3</sub> might be in the torus; WA<sub>4</sub> likely resides between the outer torus and the

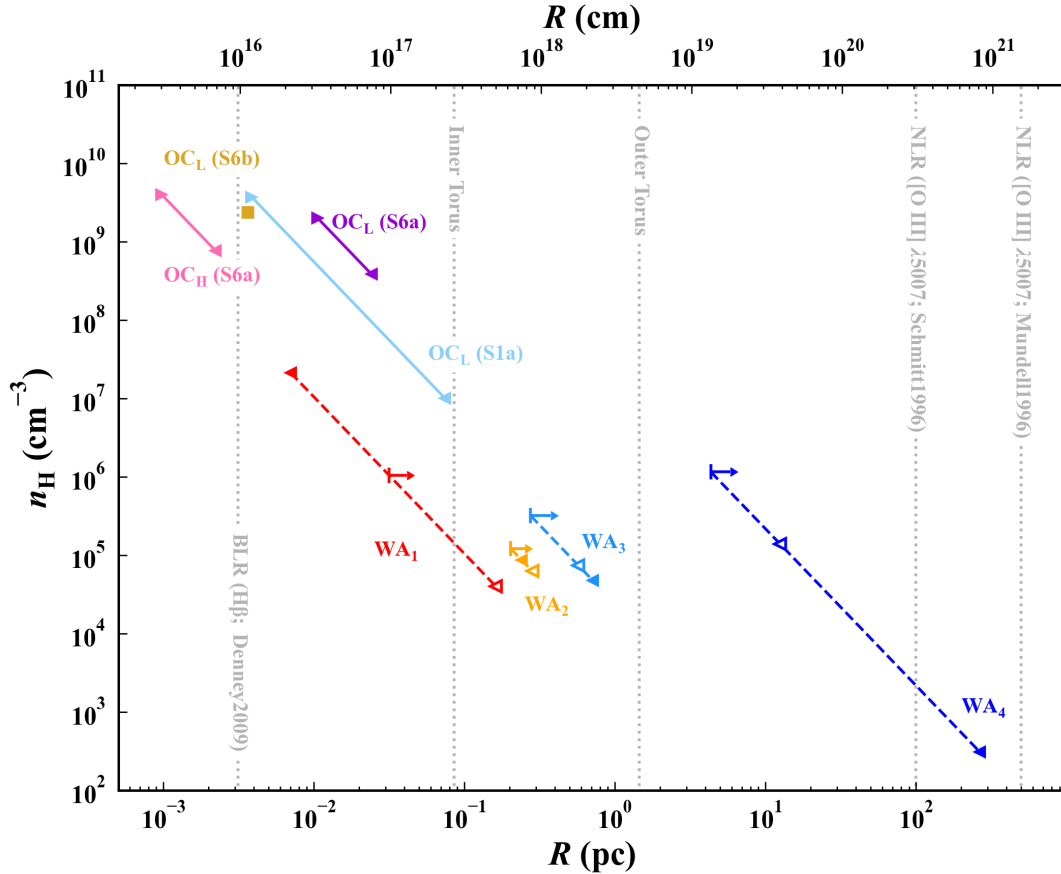


**Fig. 6.** Distances of the four WAs ( $WA_1$ ,  $WA_2$ ,  $WA_3$ ,  $WA_4$ ) and four obscurer components from the center of NGC 3227. Here,  $OC_L$  is the low-ionization obscurer component and  $OC_H$  is the high-ionization obscurer component. The symbols “◀” for the WAs represent the upper limits of the distance estimated by the assumption that the thickness of the WA cloud does not exceed its distance to the SMBH (see Eq. (2)). The symbols “↔” for the WAs represent the lower limits of the distance estimated by the assumption that the outflow velocities of winds are larger than or equal to their escape velocities (see Eq. (6)). The symbols “◁” for the WAs represent the upper limits of the distance estimated by the upper limits of the recombination timescale (see Eq. (7)). The symbols “▶” and “◀” for the obscurer components represent the lower and upper limits of the distance estimated by the range of the crossing time (see Eq. (10)). The radial location of the optical BLR of NGC 3227 is estimated by the time lag between the  $H\beta$  line and continuum at  $5100 \text{ \AA}$  (Denney et al. 2009). The inner radii of the torus are estimated by the dust sublimation radius (see Eq. (8)) and its outer radii are estimated by  $R_{\text{out}} = Y \times R_{\text{in}}$  ( $Y = 17$  for NGC 3227; Alonso-Herrero et al. 2011). The location of the NLR is estimated by the optical [O III]  $\lambda 5007$  image (Mundell et al. 1995; Schmitt & Kinney 1996).

NLR, and it is the one that is farthest away from the AGN compared with other WAs, which might explain the lowest ionization parameter of this component (see details in Sect. 4.2.1 and Table 3). For the distance estimation of  $WA_1$ , the first and second methods give inconsistent results, which might be due to the following reasons: (1) these two methods use different assumptions, which can be expected to have different results; (2) we did not consider the possible contribution from the momentum associated with other processes (e.g., magnetic field), which might not be negligible for  $WA_1$  and might lead to an underestimation for  $C_v$  (see Eq. (3)) and  $r_{\text{max}}$  (see Eq. (2)).

#### 4.3. Obscurer components

According to the softness ratio (see Sect. 3), S6a, S6b, and S1a seem to be in obscured states, which may be caused by the clouds (obscurer components) crossing the line of sight. Then we make detailed spectral modeling to check whether the obscurer components are required to explain the significant spectral variation in these slices. Firstly, we fixed the parameters of the intrinsic SED and WAs of S1a to those of S1b that is in the unobscured state because we do not expect strong variabilities in the SED

shape and WAs parameters on small time scales between S1a and S1b. However, the absorption features in the soft X-rays cannot be explained by WAs alone. Therefore, we add an obscurer component, which greatly improves the fitting result ( $\Delta C \sim 785$ ). Similarly, we firstly fixed the intrinsic SED and WAs parameters of S6b to those of S6c that is in the unobscured state. One obscurer component is also required to improve the fitting result with  $\Delta C \sim 1218$ . Adding a second obscurer component cannot improve the fitting result of both S1a and S6b. For S6a, we firstly fixed its intrinsic SED and WAs parameters to those of S6c, which cannot explain the observational data well. We verified that two obscurer components are required to improve the fitting result:  $\Delta C \sim 13582$  for adding one obscurer component and  $\Delta C \sim 31$  for adding a second obscurer component.

##### 4.3.1. Parameters of the obscurer components

The spectral analysis indicates that S6a has two obscurer components: a high-ionization component ( $\log \xi = 2.81^{+0.15}_{-0.04}$ ; S6a  $OC_H$ ) with  $C_f$  of  $0.29^{+0.04}_{-0.08}$  and a low-ionization component ( $\log \xi = 1.02^{+0.25}_{-0.14}$ ; S6a  $OC_L$ ) with  $C_f$  of  $0.46 \pm 0.03$ . S6b and

**Table 5.** Best-fit parameters of the obscurer components for S6a, S6b, and S1a: hydrogen column density ( $N_{\text{H}}$ ), ionization parameter ( $\xi$ ), covering factor ( $C_{\text{f}}$ ).

Comp.	Parameter	S6a	S6b	S1a
OC <sub>H</sub>	$N_{\text{H}}$ ( $10^{22}$ cm <sup>-2</sup> )	$8.27^{+7.28}_{-1.63}$	...	...
	$\log \xi$ (erg cm s <sup>-1</sup> )	$2.81^{+0.15}_{-0.04}$	...	...
	$C_{\text{f}}$	$0.29^{+0.04}_{-0.08}$	...	...
OC <sub>L</sub>	$N_{\text{H}}$ ( $10^{22}$ cm <sup>-2</sup> )	$1.25^{+0.32}_{-0.20}$	$1.33^{+0.27}_{-0.21}$	$1.98^{+0.59}_{-0.42}$
	$\log \xi$ (erg cm s <sup>-1</sup> )	$1.02^{+0.25}_{-0.14}$	$1.89 \pm 0.11$	$1.55^{+0.19}_{-0.30}$
	$C_{\text{f}}$	$0.46 \pm 0.03$	$0.35 \pm 0.03$	$0.21 \pm 0.02$

**Notes.** OC<sub>L</sub> is the low-ionization obscurer component and OC<sub>H</sub> is the high-ionization obscurer component.

S1a only have one low-ionization obscurer component, respectively:  $\log \xi = 1.89 \pm 0.11$  for S6b OC<sub>L</sub> with  $C_{\text{f}}$  of  $0.35 \pm 0.03$  and  $\log \xi = 1.55^{+0.19}_{-0.30}$  for S1a OC<sub>L</sub> with  $C_{\text{f}}$  of  $0.21 \pm 0.02$  (see Table 5). The low-ionization obscurer component (OC<sub>L</sub>) has a lower column density ( $\sim 10^{22}$  cm<sup>-2</sup>) than the high-ionization obscurer component (OC<sub>H</sub>;  $N_{\text{H}} \sim 10^{23}$  cm<sup>-2</sup>) (see Table 5). S6a OC<sub>L</sub> has a larger covering factor than S6a OC<sub>H</sub>, considering  $1\sigma$  level uncertainties. Our result for S6a is not consistent with that in Turner et al. (2018), which only found one obscurer component with  $N_{\text{H}} \sim 10^{22}$  cm<sup>-2</sup>,  $\log \xi \sim 2$ , and  $C_{\text{f}} \sim 60\%$ . It might be due to the different SED model and different spectral modeling process. The X-ray transmission of each obscurer component in our line of sight to NGC 3227 is shown in Fig. 5. The OC<sub>L</sub> components can produce absorption features at energies lower than 6 keV, and the OC<sub>H</sub> component mainly absorbs the continuum at energies higher than 0.5 keV.

#### 4.3.2. Radial location of the obscurer components

As we mention in Sect. 3.3, we cannot constrain the outflow velocities of the obscurer components, so we cannot estimate the distance of the obscurer components using the same methods as for the WAs. Here, we estimate the distance of the obscurer components based on the crossing time of the obscuring cloud. For simplicity, we assume that an obscuring cloud moves around the central black hole ( $M_{\text{BH}}$ ) in a circular orbit of radius  $R$ , so that the keplerian velocity of the obscuring cloud crossing the line of sight is  $v_{\text{cloud}} = \sqrt{GM_{\text{BH}}/R}$ . Assuming a spherical geometry for the obscuring cloud, its diameter is  $D \sim N_{\text{H}}/n_{\text{H}}$  and the size of this cloud crossing the line of sight is approximately equal to  $D$ , so that  $v_{\text{cloud}}$  can also be given by  $v_{\text{cloud}} = D/t_{\text{cross}} = N_{\text{H}}/(n_{\text{H}}t_{\text{cross}})$ , where  $t_{\text{cross}}$  is the crossing time of the obscuring cloud. Therefore, we can obtain a relation for  $n_{\text{H}}$ :

$$n_{\text{H}} = \frac{N_{\text{H}}}{t_{\text{cross}}} \sqrt{\frac{R}{GM_{\text{BH}}}}. \quad (9)$$

Following Lamer et al. (2003), we combine Eqs. (1) and (9) to obtain  $R$ :

$$R = 4 \times 10^{16} M_7^{1/5} \left( \frac{L_{42} t_{\text{days}}}{N_{22} \xi} \right)^{2/5} \text{ cm}, \quad (10)$$

where  $M_7 = M_{\text{BH}}/10^7 M_{\odot}$ ,  $L_{42} = L_{\text{ion}}/10^{42}$  erg s<sup>-1</sup>,  $t_{\text{days}}$  is  $t_{\text{cross}}$  in days, and  $N_{22} = N_{\text{H}}/10^{22}$  cm<sup>-2</sup>.

On the one hand, Obs5 is in an unobscured state, which indicates that OC<sub>H</sub> and OC<sub>L</sub> of S6a do not start to cross the line

**Table 6.** Crossing time ( $t_{\text{cross}}$ ) and distances ( $R$ ) of the obscurer components for S6a, S6b, and S1a.

Comp.	$t_{\text{cross}}$	$R$ (pc)
S6a OC <sub>H</sub>	39–305 ks	0.001–0.002
S6a OC <sub>L</sub>	39–305 ks	0.011–0.02
S6b OC <sub>L</sub>	$\sim 20$ ks	$\sim 0.004$
S1a OC <sub>L</sub>	20 ks–372 days	0.004–0.07

of sight during the observational time of Obs5. On the other hand, OC<sub>H</sub> of S6a disappears in the observational time of S6b. Therefore,  $t_{\text{cross}}$  of OC<sub>H</sub> should be larger than the exposure time of S6a (39 ks) and smaller than the time interval between Obs5 and Obs6 (309 ks). If we assume that S6a and S6b have different OC<sub>L</sub> components,  $t_{\text{cross}}$  of S6a OC<sub>L</sub> should be also between 39 and 309 ks (similar to the case of S6a OC<sub>H</sub>), and  $t_{\text{cross}}$  of S6b OC<sub>L</sub> should be comparable to the exposure time of S6b (20 ks). Similarly,  $t_{\text{cross}}$  of S1a OC<sub>L</sub> should be larger than the exposure time of S1a (20 ks), and smaller than the time interval (372 days) between Obs1 and an unobscured observation taken in November 2005 (see Fig. A.12 of Markowitz et al. 2014). The estimated crossing time of each obscurer component is summarized in Table 6. Then, we can use Eq. (10) to constrain the location of each obscurer component, which is shown in Table 6 and Fig. 6. These obscurer components are estimated to be located within the BLR, which is consistent with the results in previous works (Lamer et al. 2003; Beuchert et al. 2015; Turner et al. 2018).

The obscurers of NGC 3227 are closer to the SMBH than the WAs and also have a significantly larger hydrogen or electron number density than the WAs (see Fig. 6). Besides that, the obscurers usually appear on a short timescale while WAs can exist for a long time, and the appearance of the obscurers mainly affects the ionization state of the WAs on the short timescale. These results indicate that the obscurers and WA outflows might have different origins. For example, obscurers might be triggered by the collapse of inner BLR clouds (Kriss et al. 2019a,b; Devereux 2021), while WA outflows might be formed by the outflowing of the clouds between outer BLR and NLR under the drive of the radiation pressure (e.g., Proga & Kallman 2004), magnetic forces (e.g., Blandford & Payne 1982; Konigl & Kartje 1994; Fukumura et al. 2010), or thermal pressure (e.g., Begelman et al. 1983; Krolik & Kriss 1995; Mizumoto et al. 2019). However, we cannot get a solid conclusion in this work, which might require more high-quality data to investigate.

## 5. Summary and conclusions

The relationship between WA outflows of AGN and nuclear obscuration activities remains unclear. We find that NGC 3227 is a suitable target for the study of the properties of both WAs and obscurers, which might help us understand their correlation. To investigate the WA components of NGC 3227 in detail, we used a broadband SED model (Paper I) and the photoionization model in SPEX software to fit the unobscured spectra of the archival and previously published *XMM-Newton* and *NuSTAR* observations taken in 2006 and 2016. Based on the broadband SED and WAs parameters, we also study the X-ray obscuration events in the archival observations.



We detect four ionization phases for the WAs in NGC 3227 using the unobscured observations:  $\log \xi$  (erg cm s<sup>-1</sup>)  $\sim -1.0, 2.0, 2.5, 3.0$ . The highest-ionization WA component has a much higher hydrogen column density ( $N_{\text{H}} \sim 10^{22}$  cm<sup>-2</sup>) than the other three WA components ( $N_{\text{H}} \sim 10^{21}$  cm<sup>-2</sup>). The outflow velocities of these WA components range from  $\sim 100$  to  $\sim 1300$  km s<sup>-1</sup>, and show a positive correlation with the ionization parameter. Our estimates of the radial location of these WA components indicate that the WAs of NGC 3227 might reside over radii ranging from the BLR to the torus – even up to the NLR.

We find an obscuration event in 2006, which was missed by previous studies. One obscurer component is required for this 2006 obscuration event. For the previously published obscuration event in 2016, we detect two obscurer components. A high-ionization obscurer component ( $\log \xi = 2.81^{+0.15}_{-0.04}$ ; covering factor  $C_f = 0.29^{+0.04}_{-0.08}$ ) only appears in the 2016 observation, which has a column density around  $10^{23}$  cm<sup>-2</sup>, while both the 2006 and 2016 observations have a low-ionization obscurer component ( $\log \xi \sim 1.0-1.9$ ;  $C_f \sim 0.2-0.5$ ), which has a lower column density ( $\sim 10^{22}$  cm<sup>-2</sup>) than the high-ionization obscurer component. Assuming that the variations of flux is caused by the transverse motion of obscurers across the line of sight, we estimate the locations of the obscurers to be within the BLR.

The obscurers of NGC 3227 are closer to the SMBH than the WAs and have a significantly larger hydrogen or electron number density than the WAs. In addition, the obscurers usually appear on a short timescale while the WAs have the capacity to exist for a long time. These proofs indicate that the obscurers and WAs of NGC 3227 might have different origins.

**Acknowledgements.** We thank the referee for helpful comments that improved this paper. This research has made use of the NASA/IPAC Extragalactic Database (NED), which is funded by the National Aeronautics and Space Administration and operated by the California Institute of Technology. YJW gratefully acknowledges the financial support from the China Scholarship Council. YJW and YQX acknowledge support from NSFC-12025303, 11890693, 11421303, the CAS Frontier Science Key Research Program (QYZDJ-SSW-SLH006), the K.C. Wong Education Foundation, and the science research grants from the China Manned Space Project with NO. CMS-CSST-2021-A06. SRON is supported financially by NWO, the Netherlands Organization for Scientific Research. JM acknowledges the support from STFC (UK) through the University of Strathclyde UK APAP network grant ST/R000743/1. GP acknowledges funding from the European Research Council (ERC) under the European Union’s Horizon 2020 research and innovation programme (grant agreement No 865637). E.B. is funded by a Center of Excellence of THE ISRAEL SCIENCE FOUNDATION (grant No. 2752/19). SB acknowledges financial support from ASI under grants ASI-INAF I/037/12/0 and n. 2017-14-H.O., and from PRIN MIUR project “Black Hole winds and the Baryon Life Cycle of Galaxies: the stone-guest at the galaxy evolution supper”, contract no. 2017PH3WAT. BDM acknowledges support via Ramón y Cajal Fellowship RYC2018-025950-I. SGW acknowledges the support of a PhD studentship awarded by the UK Science & Technology Facilities Council (STFC). DJW acknowledges support from STFC in the form of an Ernest Rutherford fellowship. P.O.P. acknowledges financial support from the CNES french agency and the PNHE high energy national program of CNRS.

## References

Alonso-Herrero, A., Ramos Almeida, C., Mason, R., et al. 2011, *ApJ*, **736**, 82  
 Begelman, M. C., McKee, C. F., & Shields, G. A. 1983, *ApJ*, **271**, 70  
 Bentz, M. C., & Katz, S. 2015, *PASP*, **127**, 67  
 Beuchert, T., Markowitz, A. G., Krauß, F., et al. 2015, *A&A*, **584**, A82  
 Beuchert, T., Markowitz, A. G., Dauser, T., et al. 2017, *A&A*, **603**, A50  
 Blandford, R. D., & Payne, D. G. 1982, *MNRAS*, **199**, 883  
 Blustin, A. J., Page, M. J., Fuerst, S. V., Branduardi-Raymont, G., & Ashton, C. E. 2005, *A&A*, **431**, 111  
 Botorff, M. C., Korista, K. T., & Shlosman, I. 2000, *ApJ*, **537**, 134

Crenshaw, D. M., Kraemer, S. B., & George, I. M. 2003, *ARA&A*, **41**, 117  
 De Marco, B., Adhikari, T. P., Ponti, G., et al. 2020, *A&A*, **634**, A65  
 Denney, K. D., Peterson, B. M., Pogge, R. W., et al. 2009, *ApJ*, **704**, L80  
 Devereux, N. 2021, *MNRAS*, **500**, 786  
 Ebrero, J., Kaastra, J. S., Kriss, G. A., de Vries, C. P., & Costantini, E. 2013, *MNRAS*, **435**, 3028  
 Ebrero, J., Kriss, G. A., Kaastra, J. S., & Ely, J. C. 2016a, *A&A*, **586**, A72  
 Ebrero, J., Kaastra, J. S., Kriss, G. A., et al. 2016b, *A&A*, **587**, A129  
 Elvis, M. 2000, *ApJ*, **545**, 63  
 Fukumura, K., Kazanas, D., Contopoulos, I., & Behar, E. 2010, *ApJ*, **715**, 636  
 Gibson, R. R., Jiang, L., Brandt, W. N., et al. 2009, *ApJ*, **692**, 758  
 Grafton-Waters, S., Branduardi-Raymont, G., Mehdipour, M., et al. 2020, *A&A*, **633**, A62  
 Halpern, J. P. 1984, *ApJ*, **281**, 90  
 Kaastra, J. S. 2017, *A&A*, **605**, A51  
 Kaastra, J. S., Mewe, R., & Nieuwenhuijzen, H. 1996, *UV and X-ray Spectroscopy of Astrophysical and Laboratory Plasmas*, 411  
 Kaastra, J. S., Mewe, R., Liedahl, D. A., Komossa, S., & Brinkman, A. C. 2000, *A&A*, **354**, L83  
 Kaastra, J. S., Kriss, G. A., Cappi, M., et al. 2014, *Science*, **345**, 64  
 Kaastra, J. S., Mehdipour, M., Behar, E., et al. 2018, *A&A*, **619**, A112  
 Kaastra, J. S., Raassen, A. J. J., de Plaa, J., & Gu, L. 2020, <https://doi.org/10.5281/zenodo.4384188>  
 Kara, E., Mehdipour, M., Kriss, G. A., et al. 2021, *ApJ*, **922**, 151  
 King, A., & Pounds, K. 2015, *ARA&A*, **53**, 115  
 Komossa, S., & Fink, H. 1997, *A&A*, **327**, 483  
 Konigl, A., & Kartje, J. F. 1994, *ApJ*, **434**, 446  
 Kriss, G. A., Mehdipour, M., Kaastra, J. S., et al. 2019a, *A&A*, **621**, A12  
 Kriss, G. A., De Rosa, G., Ely, J., et al. 2019b, *ApJ*, **881**, 153  
 Krolik, J. H., & Kriss, G. A. 1995, *ApJ*, **447**, 512  
 Krolik, J. H., & Kriss, G. A. 2001, *ApJ*, **561**, 684  
 Krongold, Y., Nicastro, F., Elvis, M., et al. 2007, *ApJ*, **659**, 1022  
 Laha, S., Guainazzi, M., Dewangan, G. C., Chakravorty, S., & Kembhavi, A. K. 2014, *MNRAS*, **441**, 2613  
 Laha, S., Reynolds, C. S., Reeves, J., et al. 2021, *Nat. Astron.*, **5**, 13  
 Lamer, G., Uttley, P., & McHardy, I. M. 2003, *MNRAS*, **342**, L41  
 Loders, K., Palme, H., & Gail, H. P. 2009, *Landolt Börnstein*, **4B**, 712  
 Lohfink, A. M., Reynolds, C. S., Mushotzky, R. F., & Wilms, J. 2012, *ApJ*, **749**, L31  
 Longinotti, A. L., Krongold, Y., Kriss, G. A., et al. 2013, *ApJ*, **766**, 104  
 Mao, J., & Kaastra, J. 2016, *A&A*, **587**, A84  
 Mao, J., Kaastra, J. S., Mehdipour, M., et al. 2018, *A&A*, **612**, A18  
 Markowitz, A., & Edelson, R. 2004, *ApJ*, **617**, 939  
 Markowitz, A., Reeves, J. N., George, I. M., et al. 2009, *ApJ*, **691**, 922  
 Markowitz, A. G., Krumpke, M., & Nikutta, R. 2014, *MNRAS*, **439**, 1403  
 Mehdipour, M., Kaastra, J. S., & Kallman, T. 2016, *A&A*, **596**, A65  
 Mehdipour, M., Kaastra, J. S., Kriss, G. A., et al. 2017, *A&A*, **607**, A28  
 Mehdipour, M., Kriss, G. A., Kaastra, J. S., et al. 2021, *A&A*, **652**, A150  
 Mizumoto, M., Done, C., Tomaru, R., & Edwards, I. 2019, *MNRAS*, **489**, 1152  
 Mundell, C. G., Holloway, A. J., Pedlar, A., et al. 1995, *MNRAS*, **275**, 67  
 Murphy, E. M., Lockman, F. J., Laor, A., & Elvis, M. 1996, *ApJS*, **105**, 369  
 Murray, N., Chiang, J., Grossman, S. A., & Voit, G. M. 1995, *ApJ*, **451**, 498  
 Nenkova, M., Ivezić, Ž., & Elitzur, M. 2002, *ApJ*, **570**, L9  
 Nenkova, M., Sirocky, M. M., Nikutta, R., Ivezić, Ž., & Elitzur, M. 2008a, *ApJ*, **685**, 160  
 Nenkova, M., Sirocky, M. M., Ivezić, Ž., & Elitzur, M. 2008b, *ApJ*, **685**, 147  
 Newman, J., Tsuruta, S., Liebmann, A. C., Kunieda, H., & Haba, Y. 2021, *ApJ*, **907**, 45  
 Parker, M. L., Longinotti, A. L., Schartel, N., et al. 2019, *MNRAS*, **490**, 683  
 Peretz, U., & Behar, E. 2018, *MNRAS*, **481**, 3563  
 Ponti, G., Miniutti, G., Cappi, M., et al. 2006, *MNRAS*, **368**, 903  
 Porquet, D., Reeves, J. N., O’Brien, P., & Brinkmann, W. 2004, *A&A*, **422**, 85  
 Proga, D., & Kallman, T. R. 2004, *ApJ*, **616**, 688  
 Proga, D., Stone, J. M., & Kallman, T. R. 2000, *ApJ*, **543**, 686  
 Reynolds, C. S. 1997, *MNRAS*, **286**, 513  
 Reynolds, C. S., & Fabian, A. C. 1995, *MNRAS*, **273**, 1167  
 Risaliti, G., Elvis, M., Fabbiano, G., et al. 2007, *ApJ*, **659**, L111  
 Rivers, E., Risaliti, G., Walton, D. J., et al. 2015, *ApJ*, **804**, 107  
 Rybicki, G. B., & Lightman, A. P. 1979, *Radiative Processes in Astrophysics* (New York: Wiley)  
 Schmitt, H. R., & Kinney, A. L. 1996, *ApJ*, **463**, 498  
 Sobolewska, M. A., & Papadakis, I. E. 2009, *MNRAS*, **399**, 1597  
 Soldi, S., Beckmann, V., Baumgartner, W. H., et al. 2014, *A&A*, **563**, A57  
 Tarter, C. B., Tucker, W. H., & Salpeter, E. E. 1969, *ApJ*, **156**, 943  
 Tombesi, F., Cappi, M., Reeves, J. N., et al. 2010, *A&A*, **521**, A57  
 Tombesi, F., Cappi, M., Reeves, J. N., & Baito, V. 2012, *MNRAS*, **422**, L1



- Tombesi, F., Cappi, M., Reeves, J. N., et al. 2013, *MNRAS*, **430**, 1102  
 Trump, J. R., Hall, P. B., Reichard, T. A., et al. 2006, *ApJS*, **165**, 1  
 Turner, T. J., Reeves, J. N., Braito, V., et al. 2018, *MNRAS*, **481**, 2470  
 Walton, D. J., Risaliti, G., Harrison, F. A., et al. 2014, *ApJ*, **788**, 76  
 Weymann, R. J., Carswell, R. F., & Smith, M. G. 1981, *ARA&A*, **19**, 41  
 Woo, J.-H., & Urry, C. M. 2002, *ApJ*, **579**, 530
- 
- <sup>1</sup> Leiden Observatory, Leiden University, Niels Bohrweg 2, 2300 RA Leiden, The Netherlands  
 e-mail: [Y.Wang@sron.nl](mailto:Y.Wang@sron.nl)
- <sup>2</sup> SRON Netherlands Institute for Space Research, Niels Bohrweg 4, 2333 CA Leiden, The Netherlands
- <sup>3</sup> CAS Key Laboratory for Research in Galaxies and Cosmology, Department of Astronomy, University of Science and Technology of China, Hefei 230026, PR China
- <sup>4</sup> School of Astronomy and Space Science, University of Science and Technology of China, Hefei 230026, PR China
- <sup>5</sup> Department of Astronomy, Nanjing University, Nanjing 210093, PR China
- <sup>6</sup> Key Laboratory of Modern Astronomy and Astrophysics (Nanjing University), Ministry of Education, Nanjing 210093, PR China
- <sup>7</sup> Department of Physical, Hiroshima University, 1-3-1 Kagamiyama, HigashiHiroshima, Hiroshima 739-8526, Japan
- <sup>8</sup> Department of Physics, University of Strathclyde, Glasgow G4 0NG, UK
- <sup>9</sup> Anton Pannekoek Astronomical Institute, University of Amsterdam, PO Box 94249, 1090 GE Amsterdam, The Netherlands
- <sup>10</sup> Space Telescope Science Institute, 3700 San Martin Drive, Baltimore, MD 21218, USA
- <sup>11</sup> INAF-IASF Palermo, Via U. La Malfa 153, 90146 Palermo, Italy
- <sup>12</sup> INAF-Osservatorio Astronomico di Brera, Via E. Bianchi 46, 23807 Merate, LC, Italy
- <sup>13</sup> MAX-Planck-Institut für Extraterrestrische Physik, Giessenbachstrasse, 85748 Garching, Germany
- <sup>14</sup> Department of Physics, Technion-Israel Institute of Technology, 32000 Haifa, Israel
- <sup>15</sup> Dipartimento di Matematica e Fisica, Università degli Studi Roma Tre, Via della Vasca Navale 84, 00146 Roma, Italy
- <sup>16</sup> Mullard Space Science Laboratory, University College London, Holmbury St. Mary, Dorking, Surrey RH5 6NT, UK
- <sup>17</sup> Departament de Física, EEBE, Universitat Politècnica de Catalunya, Av. Eduard Maristany 16, 08019 Barcelona, Spain
- <sup>18</sup> Univ. Grenoble Alpes, CNRS, IPAG, 38000 Grenoble, France
- <sup>19</sup> Telespazio UK for the European Space Agency (ESA), European Space Astronomy Centre (ESAC), Camino Bajo del Castillo, s/n, 28692 Villanueva de la Cañada, Madrid, Spain
- <sup>20</sup> Institute of Astronomy, University of Cambridge, Madingley Road, Cambridge CB3 0HA, UK
- <sup>21</sup> School of Physics and Astronomy and Wise Observatory, Tel Aviv University, Tel Aviv 69978, Israel
- <sup>22</sup> Department of Astronomy, University of Geneva, 16 Ch. d'Ecogia, 1290 Versoix, Switzerland
- <sup>23</sup> Italian Space Agency (ASI), Via del Politecnico snc, 00133 Roma, Italy